ACS APPLIED MATERIALS & INTERFACES

Research Article

www.acsami.org

Enhanced Magnetic Fluid Hyperthermia by Micellar Magnetic Nanoclusters Composed of $Mn_xZn_{1-x}Fe_2O_4$ Nanoparticles for Induced Tumor Cell Apoptosis

Yang Qu,[†] Jianbo Li,*[,†,‡] Jie Ren,*[,†,‡] Junzhao Leng,[†] Chao Lin,[§] and Donglu Shi[§,∥]

[†]Institute of Nano and Biopolymeric Materials, School of Materials Science and Engineering, Tongji University, 4800 Caoan Road, Shanghai 201804, China

[‡]Key Laboratory of Advanced Civil Engineering Materials (Tongji University), Ministry of Education, Shanghai 201804, China

[§]Key Laboratory of Basic Research in Cardiology, Ministry of Education, Shanghai East Hospital, Institute for Biomedical Engineering and Nano Science, School of Medicine, Tongji University, Shanghai 200120, China

[∥]Materials Science and Engineering Program, Department of Mechanical and Materials Engineering, Colleague of Engineering and Applied Science, University of Cincinnati, Cincinnati, Ohio 45221-0072, United States

Supporting Information

ABSTRACT: Monodispersed $Mn_xZn_{1-x}Fe_2O_4$ magnetic nanoparticles of 8 nm are synthesized and encapsulated in amphiphilic block copolymer for development of the hydrophilic magnetic nanoclusters (MNCs). These MNCs exhibit superparamagnetic characteristics, high specific absorption rate (SAR), large saturation magnetization (M_s), excellent stability, and good biocompatibility. $MnFe_2O_4$ and $Mn_{0.6}Zn_{0.4}Fe_2O_4$ are selected as optimum compositions for the MNCs ($MnFe_2O_4$/MNC and $Mn_{0.6}Zn_{0.4}Fe_2O_4$/MNC) and employed for magnetic fluid hyperthermia (MFH) in vitro. To ensure biosafety of MFH, the parameters of alternating magnetic field (AMF) and exposure time are optimized with low frequency, f, and strength of applied magnetic field, $H_{applied}$. Under optimized conditions, MFH of $MnFe_2O_4$/MNC and $Mn_{0.6}Zn_{0.4}Fe_2O_4$/MNC result in cancer cell death rate up to 90% within 15 min. The pathway of cancer cell death is identified as apoptosis, which occurs in mild hyperthermia near 43 °C. Both $MnFe_2O_4$/MNC and $Mn_{0.6}Zn_{0.4}Fe_2O_4$/MNC show similar efficiencies on drug-sensitive and drug-resistant cancer cells. On the basis of these findings, those $Mn_xZn_{1-x}Fe_2O_4$ nanoclusters can serve as a promising candidate for effective targeting, diagnosis, and therapy of cancers. The multimodal cancer treatment is also possible as amphiphilic block copolymer can encapsulate, in a similar fashion, different nanoparticles, hydrophobic drugs, and other functional molecules.

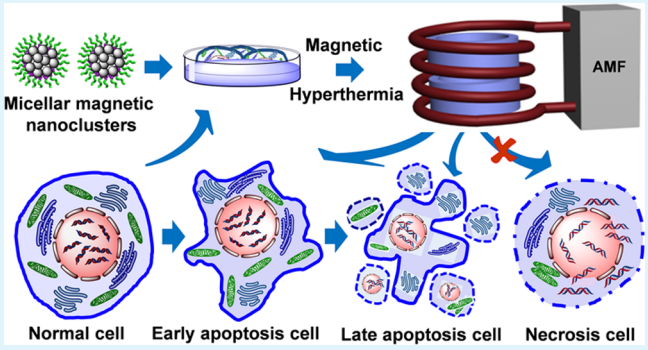

KEYWORDS: *magnetic nanoclusters, self-assembly, magnetic fluid hyperthermia, specific absorption rate, cell apoptosis*

1. INTRODUCTION

Hyperthermia is a promising tumor treatment by targeted heating of malignant tumor in the temperature range of 40.0–44.0 °C.[1] In clinic, hyperthermia has been utilized not only to kill cancer cells by denaturation and aggregation of proteins,[2] but also as an alternative treatment in combination with other established strategies, such as radiotherapy,[3] and chemotherapy.[4] In addition, hyperthermia has been used to stimulate the immune system for suppressing cancer cells.[5,6] Recently, some advances in field of photothermal treatment and magnetic fluid hyperthermia (MFH) have presented noninvasive hyperthermia, which are better options for cancer treatment than invasive heating by interstitial laser or microwave applicators.[7,8] By converting near-infrared ray (NIR) or electromagnetic energy into heat efficiently, two kinds of noninvasive hyperthermia can remotely raise temperature in tumor site without damaging the surrounding normal tissues.[9,10] However, MFH can be used in any region of body for high penetration of the magnetic field. This characteristic of MFH is advantageous when compared to depth-limited NIR of photothermal treatment.[11] Furthermore, magnetic fluid consisting of magnetic nanoparticles (MNPs) can also be used as the contrast agent in magnetic resonance imaging (MRI).[12] Therefore, versatile magnetic fluid shows a promising prospect in diagnose and treatment of cancer.[13,14]

However, a significant challenge of MFH is to improve specific absorption rate (SAR) of magnetic fluid, which represents the conversion efficiency of electromagnetic energy

Received: July 2, 2014
Accepted: September 9, 2014
Published: September 9, 2014

into thermal energy under an alternating magnetic field (AMF).[15,16] High SAR is required for generating sufficient heat with a low dosage of MNPs, a fact that is essential for ensuring curative effect and reducing the potential risk in clinical applications. To enhance SAR, previous studies have focused on relationship between composition,[17] shape,[18] and structure of MNPs and their SARs.[19] By optimizing composition, the relevant research has proved that Mn^{2+} and Zn^{2+} doped ferrite ($Mn_xZn_{1-x}Fe_2O_4$) nanoparticle showed higher SAR than MFe_2O_4 (M = Fe^{2+}, Ni^{2+}, Co^{2+}) by improving saturation magnetization (M_s) of MNPs.[17,20] Comparing with spherical MNPs, some studies have found that cubic MNPs exhibited higher SAR by enhancing their surface anisotropy (K_s).[21] At the same time, SAR of core−shell MNPs prepared by different doping ferrite was observed to be higher than that of single-component MNPs, as the former displayed exchange coupling between a magnetically hard core and magnetically soft shell.[19] Among those factors, only composition can be controlled easily by varying the initial molar ratio of the metal acetylacetonate precursors.[17,22] Comparing with composition, shape and core−shell structure of MNPs are harder to regulate. In comparison with spherical MNP, the disadvantage of cubic MNP is not only the more severe preparation condition, but the lower yield as well.[23,24] Comparing with one-pot synthesis of single-component MNP, core−shell MNP must be synthesized by two-step method, which is also called seed mediated growth,[19] as the syntheses of magnetically hard core and magnetically soft shell are separated, in which the former is seed and the latter is grown on the surface of the former.

Besides optimizing properties of single MNPs, recent advances on highly efficient MRI agents and magnetic fluids have found that magnetic nanocluster (MNC), a closed packing structure of multiple MNPs, shows higher spin−spin (T_2) relaxivity and SAR than single MNP by improving effective magnetic moment of MNP.[25−28] Although the electromagnetic energy of MNP is converted to thermal energy from the rotation of magnetic particles (Brownian relaxation) and magnetic moments within the particles (Néel relaxation) under an AMF,[29] for superparamagnetic nanoparticles with diameters around 10 nm, the heat dissipation is mainly via Néel relaxation.[30] Therefore, the SAR of MNPs around 10 nm is closely associated with their effective magnetic moment, which can be enhanced by assembling MNPs into MNCs. It also should be noted that high-quality MNPs, prepared by high-temperature solution phase reaction, are usually hydrophobic.[22] By encapsulating in the amphiphilic block copolymers, the hydrophobic MNPs can be assembled micellar MNCs with good solubility.[25] Although MNCs can be loaded by graphene oxide, which has showed enhanced T_2 relaxivity value and SAR.[31] The self-assembled MNCs by amphiphilic block copolymers can be loaded with other functional molecules easily, such as hydrophobic drug, for tumor multitreatment. $Mn_xZn_{1-x}Fe_2O_4$ nanoparticles show higher M_s and SAR than MFe_2O_4 nanoparticles around same size. Consequently, the ideal magnetic fluid is to assemble $Mn_xZn_{1-x}Fe_2O_4$ nanoparticles around 10 nm into MNCs by amphiphilic block copolymers. Those micellar MNCs can provide efficient MFH.

However, MFH of high SAR may experience overheating, raising temperature easily over 45 °C, and leading to cell necrosis. The pathways of cell death by heating were found to divide into apoptosis and necrosis in a temperature-depending manner.[32] The former, as a form of programmed cell death, generally benefits metabolism of organism and usually occurs between 42 and 44 °C in a 30 min time window. The latter is a passive pathological cell death, induced by overheating in the range of 45−47 °C for 30 min that can result in serious inflammatory and immune responses. Therefore, cell death by apoptosis is preferred in MFH therapy. Previously, we attempted to avoid overheating by preparing MNPs with low Curie point (T_c), which displayed the maximum self-heating temperature at 44.5 °C.[33] Although MFH of low T_c MNPs have safety advantages, SAR of MNPs may suffer from decreasing T_c.[34] Most of the previous research focused on improvement of SAR, but few considered the mechanisms of cell death,[21,35] which related to the safety of MFH.

In this study, we report a systemic study on a significantly improved MFH to induce cell apoptosis predominantly by a series of unique MNCs, as shown in Scheme 1. As can be seen

Scheme 1. Schematic Illustration of Effective Apoptotic Magnetic Hyperthermia by MNPs Clusters, Including the Preparation of the Micellar $Mn_xZn_{1-x}Fe_2O_4$ Nanoclusters and Cell Death Mechanism by MFH, Predominantly Cell Apoptosis at Different Exposure Times

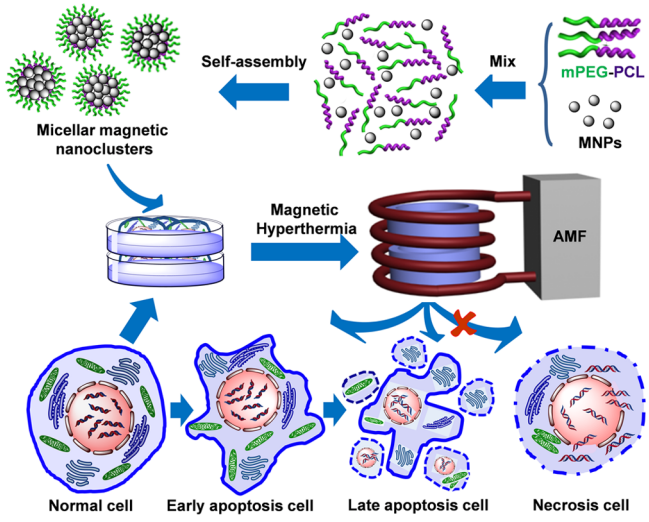

in Scheme 1, the magnetic fluid of high SAR was prepared by self-assembly of mPEG and monodisperse $Mn_xZn_{1-x}Fe_2O_4$ nanoparticles. In this fashion, the $Mn_xZn_{1-x}Fe_2O_4$ nanoclusters were encapsulated in the nanomicelles for enhanced magneto-caloric effect, good solubility and excellent biocompatibility. On the basis of the optimal $Mn_xZn_{1-x}Fe_2O_4$ clusters, the magnetocaloric effect of magnetic fluid was also studied in medium. To ensure biosafety of MFH, the AMF parameters with low frequency (f) and suitable strength of applied magnetic field ($H_{applied}$) were optimized for less exposure time according to the cell death mechanism. Theoretically, cell death should develop from early apoptosis to late apoptosis at prolonged exposure times induced by ideal MFH, without cell necrosis, as shown in Scheme 1. Under optimal conditions, the research not only promotes the antitumor efficiency of MFH on drug-sensitive cancer cell MCF-7 and drug-resistive cancer cell MCF-7/ADR, but also highlightes the cell death mechanism by MFH at different exposure times, which is identified as a promising cancer treatment integrating efficiency and safety considerations.

2. EXPERIMENTAL SECTION

2.1. Materials. Iron(III) acetylacetonate [$Fe(acac)_3$], manganese acetylacetonate [$Mn(acac)_2$], Zinc(II) acetylacetonate [$Zn(acac)_2$], benzyl ether (99%), and oleic acid (90%) were purchased from Alfa-Aesar. 1,2-Hexadecanediol (97%), oleylamine (>70%) and mPEG5k were purchased from Sigma-Aldrich. The stannous octoate ($Sn(Oct)_2$) was purchased from Tokyo Chemical Industry Co. Ltd. ε-Caprolactone was purchased from J&K Scientific Ltd. and dried with calcium hydride (CaH_2), then purified by distillation under reduced pressure before use. Dialysis tubing (MWCO: 8−14 kDa), tetrahydrofuran (THF) and dimethyl sulfoxide (DMSO) were purchased from Shanghai Chemical Reagent Co. Ltd. (China). 3-(4,5-dimethyl-thiazol-2-yl)-2,5-diphenyl tetrazolium bromide (MTT) was purchased from Sigma-Aldrich. 2-(4-Amidinophenyl)-6-indolecarbamidine dihydrochloride (DAPI) and 1,1′-dioctadecyl-3,3,3′,3′-tetramethylindocarbocyanine perchlorate (DiI) were purchased from Beyotime Biotech. Co., Ltd. (China). Isothiocyanite (FITC) labeled Annexin-V (Annexin-V-FITC) and propidium iodide (PI) (Annexin V-FITC/PI) Apoptosis Detection Kit (100 T) was purchased from KeyGen Biotech. Co. Ltd. (China). All other reagents were used as received. The water used in all experiments was deionized with a Millipore Milli-Qsystem.

2.2. Preparation of Monodisperse $Mn_xZn_{1-x}Fe_2O_4$ Nanoparticles. The monodisperse magnetic nanoparticles were synthesized following a published procedure by Sun et al.[22] Briefly, based on the theoretical element ratio of Mn/Zn/Fe in $Mn_xZn_{1-x}Fe_2O_4$ nanoparticles (x = 0, 0.2, 0.4, 0.6, 0.8, 1), $Fe(acac)_3$ (2 mmol) and certain $Mn(acac)_2$ and $Zn(acac)_2$ with corresponding moles were mixed with 1,2-hexadecanediol (10 mmol), oleic acid (6 mmol), and oleylamine (6 mmol) in benzyl ether (20 mL) under dry and deoxidized argon atmosphere. The mixture was heated to 200 °C for 2 h and then heated to reflux (≈300 °C) for 1 h. After it had cooled to room temperature, the solution was treated with ethanol and then centrifuged to yield a dark-brown precipitate. The $Mn_xZn_{1-x}Fe_2O_4$ nanoparticles were redispersed in hexane and reprecipitated with ethanol. Finally, these nanoparticles were dispersed in anhydrous hexane for storage.

2.3. Preparation of Amphiphilic Block Copolymer mPEG−PCL. Amphiphilic block copolymer mPEG−PCL was synthesized by ring-opening polymerization of ε-caprolactone using $mPEG_{5k}$ as a macroinitiator, and $Sn(Oct)_2$ as a catalyst.[36] The molar ratio of $mPEG_{5k}$/ε-caprolactone was 1/44. The whole reaction system was placed in oil bath at 110 °C for 24 h with magnetic stirring. After the reaction, the resulting block copolymers were dissolved in THF and precipitated in cold ether with 10-fold volume. Then, the precipitates were purified by reprecipitation in excess amount of cold ether three times. At last, the precipitates were dried in vacuum oven.

2.4. Preparation of Copolymer Micelles and Micellar MNCs. All micelles were prepared by self-assembly technology. For copolymer micelles, mPEG−PCL was dissolved in THF completely with the concentration of 5 mg mL^{-1}. The mixed solution was then slowly added into deionized water with sonication. The mixture was dialyzed overnight to remove THF. The micellar MNCs were prepared as follows. For micellar $Mn_{0.6}Zn_{0.4}Fe_2O_4$ nanoclusters with different mass ratios of $Mn_{0.6}Zn_{0.4}Fe_2O_4$/copolymer, $Mn_{0.6}Zn_{0.4}Fe_2O_4$, and mPEG−PCL with corresponding mass ratio (1/1, 1/2, 1/3, 1/4) were separately dissolved in THF, in which the concentration of mPEG−PCL was fixed at 5 mg mL^{-1}. The solutions were subsequently added into deionized water with sonication and dialyzed overnight to remove THF. With adjustment of mass ratio of $Mn_xZn_{1-x}Fe_2O_4$/copolymer as 1/1, other micellar $Mn_xZn_{1-x}Fe_2O_4$ nanoclusters ($Mn_xZn_{1-x}Fe_2O_4$/MNC) were prepared with the same procedure, denoted as $MnFe_2O_4$/MNC, $Mn_{0.8}Zn_{0.2}Fe_2O_4$/MNC, $Mn_{0.6}Zn_{0.4}Fe_2O_4$/MNC, $Mn_{0.4}Zn_{0.6}Fe_2O_4$/MNC, $Mn_{0.2}Zn_{0.8}Fe_2O_4$/MNC, and $ZnFe_2O_4$/MNC. All products were freeze-dried and stored under vacuum at 18 °C.

2.5. Material Characterizations. The structural formations of $Mn_xZn_{1-x}Fe_2O_4$ were characterized by X-ray diffraction (XRD) with Rigaku D/Max-2550VB3+ (Cu Kα radiation, 40 kV, 100 mA, Japan). The morphology of $Mn_xZn_{1-x}Fe_2O_4$ was characterized by high-resolution transmission electron microscopy (HRTEM, JEOL JEM-2010F, 200 kV, Japan), in which the lattice structures and element analysis of $Mn_xZn_{1-x}Fe_2O_4$ were investigated. The element atomic ratios of monodisperse $Mn_xZn_{1-x}Fe_2O_4$ nanoparticles were characterized by energy dispersive X-ray spectroscopy (EDS, an attachment of JEOL JEM-2010F) and inductively coupled plasma atomic emission spectroscopy (ICP-AES, Vista AX, Varian). The composition and structure of polymer were characterized by ^1H NMR spectrum (Bruker, DMX 500 NMR, Switzerland) with $CDCl_3$ as the solvent. The chemical shifts were relative to tetramethylsilane. The morphology of copolymer micelles and micellar MNC were observed with HRTEM after dyeing by phosphotungstic acid (PTA) solution (2 wt % in deionized water). The content of MNPs in micellar MNCs with different $Mn_{0.6}Zn_{0.4}Fe_2O_4$ loadings was characterized by thermogravimetric analysis (TGA, NETZSCH STA 449C, Germany) in the temperature range from 25 to 600 °C at the heating rate of 10 °C min^{-1}. The magnetic properties of $Mn_xZn_{1-x}Fe_2O_4$ and micellar MNCs were characterized by vibrating sample magnetometer (VSM, LakeShore 7404) at 300 K. The diameter distributions of the $Mn_{0.6}Zn_{0.4}Fe_2O_4$ particles, copolymer micelles, and micellar MNCs with different mass ratios of $Mn_{0.6}Zn_{0.4}Fe_2O_4$/copolymer were characterized by dynamic laser scattering (DLS, Malvern Autosizer 4700, U.K.) with a concentration of 0.1 mg mL^{-1}. After dispersing in deionized water, phosphate buffer solution (PBS, 1×) and normal saline (NS, 1×), the colloidal stability of micellar MNCs was investigated by qualitative observation (digital imaging) and quantitative analysis (DLS). The concentration of micellar MNCs were fixed as 0.5 mg mL^{-1}.

2.6. Magnetocaloric Effect of Micellar $Mn_xZn_{1-x}Fe_2O_4$/MNCs. To evaluate the potential of the micellar $Mn_xZn_{1-x}Fe_2O_4$/MNCs in MFH, the SARs of $Mn_xZn_{1-x}Fe_2O_4$ nanoclusters were characterized by the alternating magnetic field generator (SPG-20AB, ShuangPing Tech. Ltd., China). The f of the alternating magnetic field was fixed at 114 kHz, and the $H_{applied}$ was adjusted ranging from 0 to 115.1 kA m^{-1}. The micellar $Mn_xZn_{1-x}Fe_2O_4$/MNCs were dispersed into deionized water to form colloids with 0.1 mg mL^{-1} of $Mn_xZn_{1-x}Fe_2O_4$, in which the concentration of MNPs was quantified by ICP-AES. In all measurements, 2 mL of colloidal solutions of micellar $Mn_xZn_{1-x}Fe_2O_4$/MNCs was exposed to different $H_{applied}$ of oscillating AMF (63.6, 89.9, and 114.9 kA m^{-1}) with the same f (114 kHz) in the center of the copper coil (inner diameter of 18 mm). The temperature changes were recorded using a computer-attached fiber optic temperature sensor (FOT-M, FISO, Canada). The SAR of each sample was calculated from the following equation:[37]

$$\mathrm{SAR} = C\frac{\Delta T}{\Delta t} \times \frac{1}{m_{Fe} + m_{Mn} + m_{Zn}}$$

In this equation, C is the specific heat of deionized water (C_{water} = 4.18 J g^{-1} $°C^{1-}$), $\Delta T/\Delta t$ is the initial slope of the time-dependent temperature curve at the first 20 s, and the $m_{Fe} + m_{Mn} + m_{Zn}$ is the weight fraction of the metal element in the sample.

2.7. Cell Culture. MCF-7 and MCF-7/ADR cell lines were provided by the Institute of Biomedical Engineering & Nano Science, Tongji University (China). MCF-7 was cultured in RPMI-1640 (Gibco) containing 10% fetal bovine serum (FBS, Hyclone). MCF-7/ADR was cultured in RPMI-1640 containing 10% FBS and 0.5 μg mL^{-1} doxorubicin. These cell lines were cultured in incubator at 37 °C, 5% CO_2 and humidified environment.

2.8. Biocompatibility of Micellar $Mn_xZn_{1-x}Fe_2O_4$/MNCs. In vitro biocompatibility of micellar $Mn_xZn_{1-x}Fe_2O_4$/MNCs was assessed by MTT and observed by fluorescence imaging. For MTT, cells were incubated with $Mn_xZn_{1-x}Fe_2O_4$/MNCs in 96 well, in which the concentration of the samples varied from 0.05 to 1 mg mL^{-1}. After incubating for 48 h, cell viability was investigated by the standard MTT method.[38] In this study, culture medium was selected as control and each sample was reduplicated five times. The cell survival rate was calculated as the percentage of control values. The fluorescence imaging of MCF-7 and MCF-7/ADR was observed by a confocal laser scanning microscopy (CLSM, TCS SP, Leica, Germany). After

incubation with samples (1 mg mL^{-1}) for 48 h, cells were fixed with paraformaldehyde (4%) for 30 min in incubator. Paraformaldehyde was then removed and cells were stained by DAPI (excitation/emission: 346 nm/454 nm) solution (2 μg mL^{-1}) for 10 min initially. After removing DAPI solution, the cells were stained by DiI (excitation/emission: 549 nm/575 nm) solution (2 μg mL^{-1}) for 10 min. After dyeing, cells were washed with PBS 3 times and stored at 4 °C. The cells were imaged by CLSM with identical settings for each dye.

2.9. Magnetocaloric Effect of Micellar $Mn_xZn_{1-x}Fe_2O_4$/MNCs in Culture Medium. To optimize $H_{applied}$, the magnetocaloric effect of $MnFe_2O_4$/MNC and $Mn_{0.6}Zn_{0.4}Fe_2O_4$/MNC in culture medium was investigated. To simulate the condition of cell culture, the container of $Mn_xZn_{1-x}Fe_2O_4$/MNC was replaced with culture dish of 35 mm inner diameter. A new heating copper coil with 40 mm inner diameter was utilized in the experiment. In this study, the exposure time under AMF was prolonged to 20 min, which was longer than that for the SAR measurement.

2.10. Cytotoxicity of MFH. To evaluate the efficiency of MFH, the cytotoxicity of $MnFe_2O_4$/MNC and $Mn_{0.6}Zn_{0.4}Fe_2O_4$/MNC under AMF was investigated by MTT and also observed by fluorescence imaging. The cells were incubated in culture dish (35 mm) with $MnFe_2O_4$/MNC and $Mn_{0.6}Zn_{0.4}Fe_2O_4$/MNC (0.2 mg mL^{-1}), respectively. The cells were exposed to AMF within different time intervals of 5, 10, and 15 min. After exposure to AMF, the cells were cultured in incubator for 24 h. After incubation, cell survival was assessed by MTT quantitatively and observed by fluorescence imaging. The standard protocols are described previously in this report. The cells were stained by DAPI to distinguish the nucleus. The medium (37 °C) was selected as negative control. Mild hyperthermia (43 °C) with the same exposure time was selected as positive control. Each sample was reduplicated four times. The relative cell survival was calculated as the percentage of negative control values.

2.11. Cell Apoptosis Analysis by Flow Cytometry. The pathways of cell death were investigated by staining with Annexin-V-FITC/PI, and measured by an FACS Calibur flow cytometer (Becton Dickinson). MCF-7 and MCF-7/ADR were cultured in culture dish and treated with MFH ($MnFe_2O_4$/MNC and $Mn_{0.6}Zn_{0.4}Fe_2O_4$/MNC) and mild hyperthermia (43 °C) with the same exposure time. After treatment, the cells were cultured for 24 h again in incubator. All cells of each sample were collected, centrifuged at 800 rpm for 3 min, and washed twice with cold PBS (pH = 7.4). The cells were resuspended in 300 mL of PBS and stained by both Annexin V-FITC (5 μL) and PI (5 μL) in dark condition. After a dyeing period of 10 min, the suspended cells were directly recognized by an FACS Calibur flow cytometer. In this experiment, untreated cells were used as a blank (medium and 37 °C). For each sample, 2×10^4 cells were counted and distinguished as living cells (Annexin-V-FITC-/PI-, lower left quadrant); early stage apoptosis cells (Annexin-V-FITC+/PI-, lower right quadrant); late-stage apoptosis cells (Annexin-V-FITC+/PI+, upper right quadrant), and necrosis cells (Annexin-V-FITC-/PI+, upper left quadrant).

3. RESULTS AND DISCUSSION

3.1. Synthesis and Characterization of $Mn_xZn_{1-x}Fe_2O_4$ Nanoparticles. Following the method of solution-phase thermal decomposition,[22] monodisperse $Mn_xZn_{1-x}Fe_2O_4$ nanoparticles were synthesized. The Mn^{2+} and Zn^{2+} doping levels of $Mn_xZn_{1-x}Fe_2O_4$ were carefully controlled by varying the initial molar ratio of the metal acetylacetonate precursors. As shown in Figure 1A, the HRTEM images indicate that a series of $Mn_xZn_{1-x}Fe_2O_4$ nanoparticles are successfully obtained with a narrow size distribution around 8 nm. The HRTEM images also show well-resolved lattice fringes (in the insets of Figure 1, a–f), demonstrating high crystallinity of the $Mn_xZn_{1-x}Fe_2O_4$ nanoparticles.

The XRD results show a single-phase spinel structure of $Mn_xZn_{1-x}Fe_2O_4$. As shown in Figure 1g, the peaks at 18.5°, 30.2°, 35.6°, 43.0°, 53.4°, 57.1°, and 62.5° are well indexed to

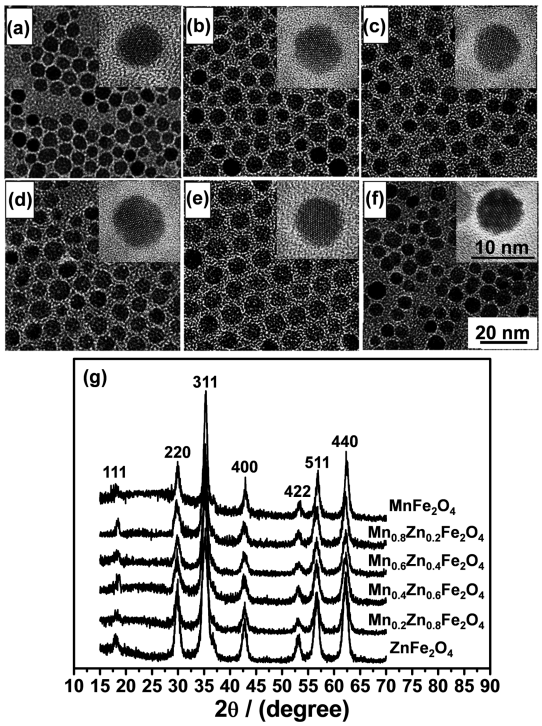

Figure 1. HRTEM (a–f) and XRD (g) result of monodisperse $Mn_xZn_{1-x}Fe_2O_4$ nanoparticles: (a) $MnFe_2O_4$, (b) $Mn_{0.8}Zn_{0.2}Fe_2O_4$, (c) $Mn_{0.6}Zn_{0.4}Fe_2O_4$, (d) $Mn_{0.4}Zn_{0.6}Fe_2O_4$, (e) $Mn_{0.2}Zn_{0.8}Fe_2O_4$, (f) $ZnFe_2O_4$, (g) XRD result of $Mn_xZn_{1-x}Fe_2O_4$ nanoparticles.

the crystal plane of spinel ferrite (111), (220), (311), (400), (422), (511), and (440), respectively. All diffraction peaks of $Mn_xZn_{1-x}Fe_2O_4$ match the corresponding JCPDS No. 10-319 for $MnFe_2O_4$, No. 74-2402 for $Mn_{0.8}Zn_{0.2}Fe_2O_4$, No. 74-2401 for $Mn_{0.6}Zn_{0.4}Fe_2O_4$, No. 74-2400 for $Mn_{0.4}Zn_{0.6}Fe_2O_4$, No. 74-2399 for $Mn_{0.2}Zn_{0.8}Fe_2O_4$, and No. 22-1012 for $ZnFe_2O_4$. The metal element ratio in the $Mn_xZn_{1-x}Fe_2O_4$ nanoparticles was assessed by EDS and ICP-AES (Supporting Information Figure S1 and Table S1).

The magnetism of MNPs with different Mn/Zn ratio was characterized by VSM at 300 K, and the results are shown in Figure 2. The hysteresis loop profiles of all MNPs exhibit superparamagnetism without significant coercivity (H_c) and remanent magnetization (M_r) (details shown in Table 1). However, the M_s values of $Mn_xZn_{1-x}Fe_2O_4$ show Mn to Zn

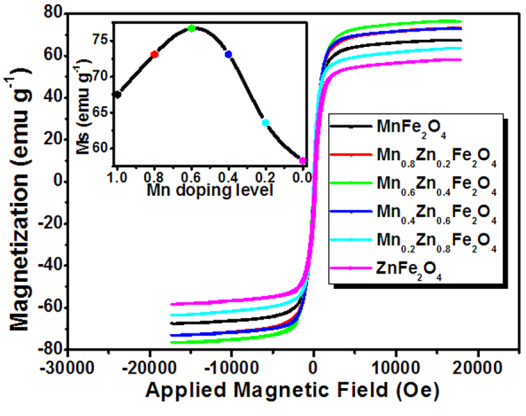

Figure 2. Magnetic hysteresis loops of the $Mn_xZn_{1-x}Fe_2O_4$ nanoparticles.

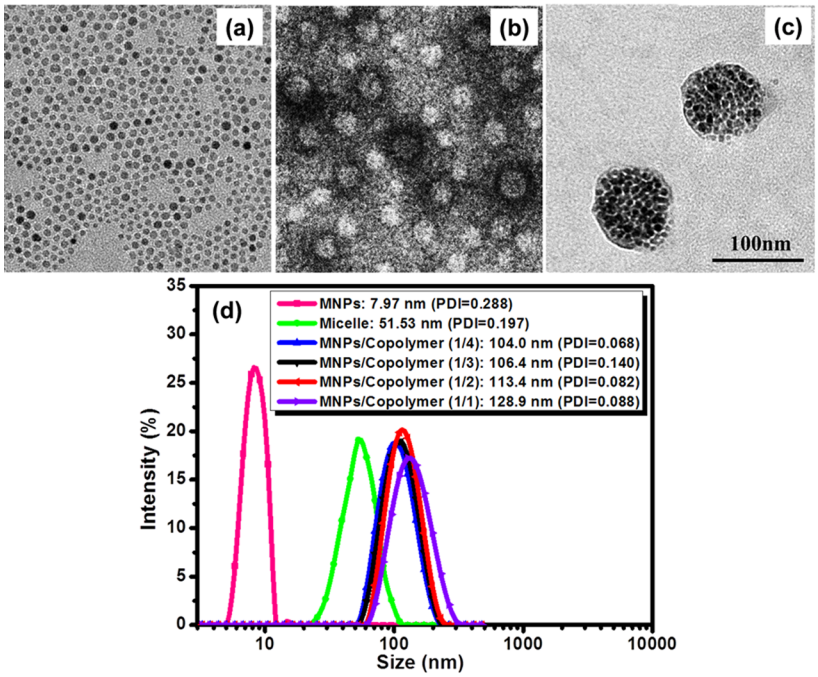

Figure 3. HRTEM and DLS results of MNPs ($Mn_{0.6}Zn_{0.4}Fe_2O_4$), copolymer micelles, and micellar MNCs: (a) HRTEM result of $Mn_{0.6}Zn_{0.4}Fe_2O_4$ nanoparticles; (b) HRTEM result of copolymer micelles, and (c) HRTEM result of micellar MNCs with 1/1 mass ratio of $Mn_{0.6}Zn_{0.4}Fe_2O_4$/copolymer; (d) DLS result of the $Mn_{0.6}Zn_{0.4}Fe_2O_4$ nanoparticles, copolymer micelles, and micellar MNCs with different $Mn_{0.6}Zn_{0.4}Fe_2O_4$/copolymer mass ratios.

ratio dependence. The M_s of $Mn_xZn_{1-x}Fe_2O_4$ gradually increases with the decrease of Mn^{2+} doping from 1 to 0.6, and reaches the maximum of 76.7 emu g^{-1}. M_s of MNPs was found to decrease, however, with further decreasing of Mn^{2+}. The similar result was found and explained by Cheon et al., by considering the coupling interactions between the Td and Oh sites modulated by Zn^{2+} dopants.[17] On the basis of their explanation, the theoretical M_s of pure $ZnFe_2O_4$ has been calculated to be zero.[39] In this study, however, M_s of pure $ZnFe_2O_4$ was shown to be 58.3 emu g^{-1}, slightly higher than that of pure Fe_3O_4 (57 emu g^{-1}) with similar size.[16] Other literature reported a M_s value of 30.8 emu g^{-1} for $ZnFe_2O_4$ of 6 nm.[26] It is likely that $ZnFe_2O_4$ was synthesized with a low Fe^{2+} doping level.[40]

3.2. Synthesis and Characterization of Amphiphilic Block Copolymer. Coated with oleic acid and oleylamine, the high quality monodispersed $Mn_xZn_{1-x}Fe_2O_4$ nanoparticles were found to be hydrophobic. To improve solubility and SAR of magnetic fluid, the amphiphilic block copolymer was synthesized to develop the micellear MNCs.

The monomethoxy-terminated poly(ethylene glycol)-*b*-poly-(*ε*-caprolactone) (mPEG−PCL) amphiphilic block copolymer was synthesized by ring opening polymerization. The polymer composition, structure, and molecular mass were characterized by ^{1}H NMR spectrum (Supporting Information Figure S2).

3.3. Self-Assembly and Optimization of Micellar MNC. The micellar MNCs, loaded with $Mn_xZn_{1-x}Fe_2O_4$ nanoparticles, were prepared by the self-assembly method (see Scheme 1). The $Mn_{0.6}Zn_{0.4}Fe_2O_4$ nanoparticles were used for the micellar MNCs for their large M_s. Because the size of MNC shows positive effect on spin−spin (T_2) relaxivity of contrast agent and SAR of magnetic fluid by improving effective magnetic moment of each MNP.[41] Logically, MNCs of larger size show more potential on enhancing SAR. Therefore, the research varied mass ratio of $Mn_{0.6}Zn_{0.4}Fe_2O_4$ and copolymer from 1/4 to 1/1, optimizing physical properties of micellar MNCs.

Figure 3 shows the HRTEM images of the $Mn_{0.6}Zn_{0.4}Fe_2O_4$ nanoparticles (Figure 3a), copolymer micelles (Figure 3b) and micellar MNCs with 1/1 mass ratio of $Mn_{0.6}Zn_{0.4}Fe_2O_4$ to copolymers (Figure 3c). As shown in this figure, the amphiphilic mPEG−PCL self-assembles into the micelles of 40 nm. The micellar MNCs are found to be spherical around 100 nm, with a core of $Mn_{0.6}Zn_{0.4}Fe_2O_4$ nanocluster and shell of mPEG−PCL. Interacting with the hydrophobic blocks of mPEG−PCL, the $Mn_{0.6}Zn_{0.4}Fe_2O_4$ nanoparticles are packed compactly to form isolated clusters as shown in Figure 3c. The result proves directly formation of MNCs by self-assembling.

Next, the DLS results, as shown in Figure 3d, indicate, respectively, the diameters of the $Mn_{0.6}Zn_{0.4}Fe_2O_4$ nanoparticles, copolymer micelles, and micellar MNCs, for mass ratios of $Mn_{0.6}Zn_{0.4}Fe_2O_4$ to copolymer as 1/1, 1/2, 1/3, and 1/4. Among them, the diameter of the $Mn_{0.6}Zn_{0.4}Fe_2O_4$ nanoparticles was consistent with the results of HRTEM (Figures 1 and 3a). The diameters of those micellar MNCs are significantly larger than those of the copolymer micelles as a result of MNPs encapsulation. However, diameters of the copolymer and micellar MNCs from the HRTEM results appear slightly smaller than those in DLS. It is possible that the hydrophilic blocks of copolymer shrink in the dry and vacuum conditions during the HRTEM experiments. Moreover, the mass ratio of MNPs/copolymers is changed from 1/4 to 1/1, and the corresponding diameter of the micellar MNCs has increased from 104.0 to 128.9 nm. Apparently, the size distribution of MNCs with different mass ratio of MNPs/copolymers is involved in the range of enhanced permeability and retention (EPR) effect (10−200 nm), and all of them can be concentrated in tumor by EPR effect.[42] However, the

diameter of micellar MNCs increases with feed ratios of MNPs in gross mass. Therefore, the high feed ration of MNPs benefits enhancement of SAR. Additionally, other properties of micellar MNCs with different mass ratios of MNPs/copolymers should be further characterized by TGA, VSM, and DLS, in order to optimize MNPs content, magnetic property, and colloidal stability.

The TGA result shows the mass variation of micellar MNC between 200 and 500 °C, in which the mass of remnants reflects the $Mn_{0.6}Zn_{0.4}Fe_2O_4$ fractions in the micellar MNC. As shown in Figure 4a, the contents of $Mn_{0.6}Zn_{0.4}Fe_2O_4$ in the

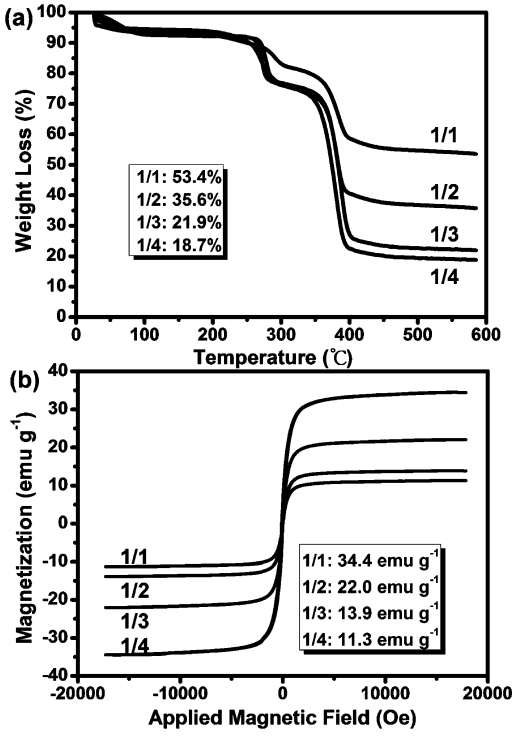

Figure 4. TGA results (a) and magnetic hysteresis loops (b) of the micellar MNCs with different mass ratios indicated.

micellar MNCs are, respectively, 53.4%, 35.6%, 21.9%, and 18.7%, for the feed ratios of MNPs in gross mass of 50%, 33%, 25%, and 20%. The $Mn_{0.6}Zn_{0.4}Fe_2O_4$ clusters exhibit superparamagnetism, as shown in Figure 4b. However, the result also shows M_s of the micellar MNCs strongly dependent on MNPs content. While M_s of the $Mn_{0.6}Zn_{0.4}Fe_2O_4$ nanoparticles is as high as 76.7 emu g^{-1}, that of the micellar MNCs decreases sharply to 34.4, 22.0, 13.9, and 11.3 emu g^{-1}, for the mass ratios of 1/1, 1/2, 1/3, and 1/4, respectively. As the magnetic targeting of MNCs in vivo depends on their M_s, the MNCs with the highest M_s and MNP content benefit their concentration in vivo.[43,44]

The effect of $Mn_{0.6}Zn_{0.4}Fe_2O_4$/copolymers mass ratio on the colloidal stability of micellar MNCs was investigated by DLS. After mixing with deionized water, the micellar MNCs with different mass ratios of MNPs/copolymers are dispersed quickly in water by slight shaking. With the same concentration (0.5 mg mL^{-1}), the colloidal solutions of micellar MNCs display brown color of different shades, corresponding to their MNPs mass fractions, as shown in Figure 5a. The colloidal stability of micelles is associated with the hydrophilic block of copolymer as the shells of MNPs clusters in deionized water.

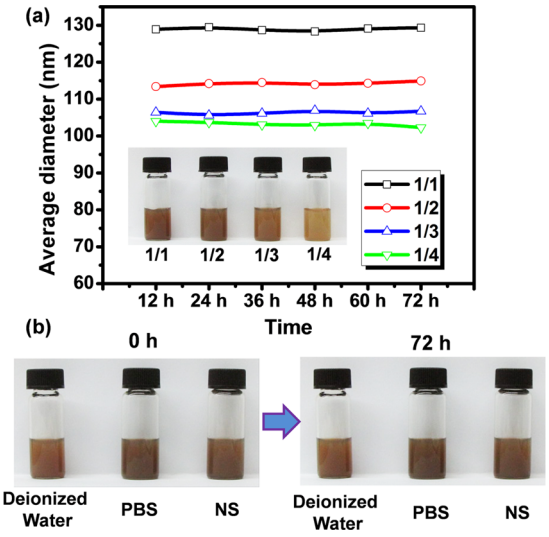

Figure 5. Colloidal stability of the micellar MNCs: (a) digital images and time-dependent average diameters of micellar MNCs with different mass ration in deionized water, (b) colloidal stability of the micellar MNCs with the $Mn_{0.6}Zn_{0.4}Fe_2O_4$/copolymers ratio of 1/1 in different mediums.

However, the time-dependent hydrodynamic diameter of the micellar MNCs in water, with different mass rations of $Mn_{0.6}Zn_{0.4}Fe_2O_4$/copolymers, does not show significant variation, as shown in Figure 5a. Thus, the colloidal stability of those micelles does not appear to be influenced by the mass ratio of MNPs/copolymers. In physiological condition, as shown in Figure 5b, 0.5 mg mL^{-1} of micellar MNCs with 1/1 of $Mn_{0.6}Zn_{0.4}Fe_2O_4$/copolymers mass ratio is found stable in water, PBS, and NS without any precipitation between 0 and 72 h. The colloidal stability of the micellar MNCs in physiological conditions was also investigated by DLS (data not shown). The hydrodynamic diameters of the micellar MNCs in PBS and NS are, respectively, similar to those in water, and not changed significantly after 72 h. The colloidal stability of the micellar MNCs in physiological condition is determined by its surface non-ionic PEG blocks.

Consequently, the 1/1 mass ratio of MNPs/copolymers was found to be optimum for micellar MNCs, because of largest size, the highest M_s and excellent colloidal stability.

3.4. Magnetocaloric Effect of the Micellar $Mn_xZn_{1-x}Fe_2O_4$/MNCs. To investigate the magnetocaloric effect of the $Mn_xZn_{1-x}Fe_2O_4$/MNCs, a series of $Mn_xZn_{1-x}Fe_2O_4$ nanoparticles were encapsulated in mPEG–PCL with 1/1 mass ratio of MNPs/copolymer.

The magnetic hysteresis loops of these $Mn_xZn_{1-x}Fe_2O_4$/MNCs are characterized by VSM, as shown in Supporting Information Figure S3. The SAR values of the $Mn_xZn_{1-x}Fe_2O_4$ clusters were investigated by measuring the temperature change of corresponding micelles in an induction heating system with 0.1 mg mL^{-1} concentration of $Mn_xZn_{1-x}Fe_2O_4$. In this study, f of the alternating magnetic field was fixed at 114 kHz, which is lower than that of most of the previously reported ones.[16−19,31]

The heating profiles of the micellar $Mn_xZn_{1-x}Fe_2O_4$/MNCs were found to be affected by the properties of $Mn_xZn_{1-x}Fe_2O_4$ clusters and $H_{applied}$. Comparing all self-heating curves of the $Mn_xZn_{1-x}Fe_2O_4$ clusters, we find the the rank of initial calefactive velocity to be $MnFe_2O_4$/MNC > $ZnFe_2O_4$/MNC > $Mn_xZn_{1-x}Fe_2O_4$/MNCs (x = 0.8−0.2). The heating profiles

measured at different $H_{applied}$ exhibited similar trends. On the basis of the initial calefactive velocity of the micellar $Mn_xZn_{1-x}Fe_2O_4$/MNCs at $H_{applied}$ of 114.9 kA m^{-1} (Figure 6c), the theoretical maximum SARs of the $Mn_xZn_{1-x}Fe_2O_4$ clusters are calculated, as shown in Table 1. In Table 1, the relevant properties of $Mn_xZn_{1-x}Fe_2O_4$ and $Mn_xZn_{1-x}Fe_2O_4$/MNC are listed including M_s, M_r and H_c. As can be seen in this table, the M_s values of $MnFe_2O_4$/MNC and $ZnFe_2O_4$/MNC are lower than those of $Mn_xZn_{1-x}Fe_2O_4$/MNCs (x = 0.8, 0.6, 0.4), but their M_r and H_c are several times higher. Consequently, the SARs of $MnFe_2O_4$/MNC and $ZnFe_2O_4$/MNC are higher than those of other $Mn_xZn_{1-x}Fe_2O_4$/MNCs. In the $Mn_xZn_{1-x}Fe_2O_4$/MNCs (x = 0.8, 0.6, 0.4, 0.2) system, $Mn_{0.6}Zn_{0.4}Fe_2O_4$/MNC exhibited the highest SAR value for its greater M_s.

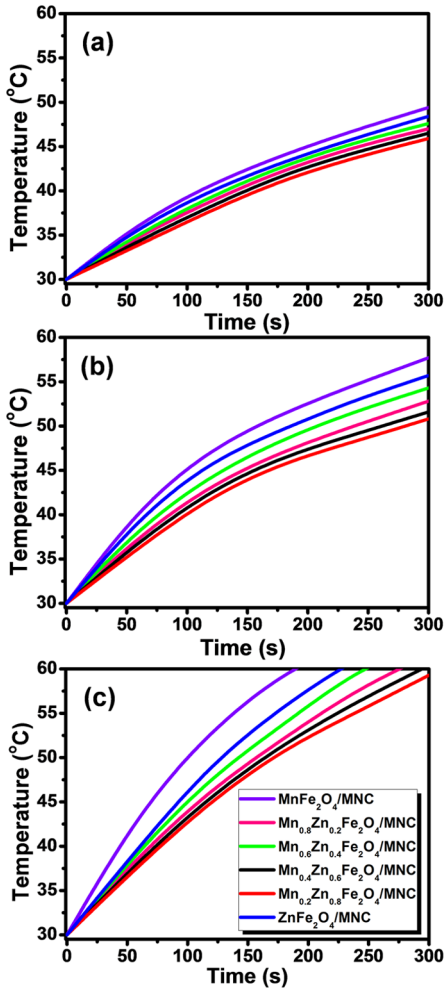

Figure 6. Time-dependent temperature curves of $Mn_xZn_{1-x}Fe_2O_4$/MNCs under AMF with f of 114 kHz and different $H_{applied}$: (a) 63.6 kA m^{-1}; (b) 89.9 kA m^{-1}, and (c) 114.9 kA m^{-1}.

Table 1. Magnetic Properties and SAR Values of $Mn_xZn_{1-x}Fe_2O_4$ and $Mn_xZn_{1-x}Fe_2O_4$/MNC

materials	M_s (emu g^{-1})	M_r (emu g^{-1})	H_c (G)	SAR (W g^{-1})
$MnFe_2O_4$	67.5	0.810	7.97	
$MnFe_2O_4$/MNC	23.7	0.129	2.30	1618.8
$Mn_{0.8}Zn_{0.2}Fe_2O_4$	73.1	0.181	1.81	
$Mn_{0.8}Zn_{0.2}Fe_2O_4$/MNC	25.9	0.052	0.82	1037.8
$Mn_{0.6}Zn_{0.4}Fe_2O_4$	76.7	0.127	1.47	
$Mn_{0.6}Zn_{0.4}Fe_2O_4$/MNC	34.5	0.034	0.89	1102.4
$Mn_{0.4}Zn_{0.6}Fe_2O_4$	73.1	0.140	1.37	
$Mn_{0.4}Zn_{0.6}Fe_2O_4$/MNC	25.3	0.055	0.89	962.0
$Mn_{0.2}Zn_{0.8}Fe_2O_4$	63.6	0.123	0.84	
$Mn_{0.2}Zn_{0.8}Fe_2O_4$/MNC	21.3	0.032	0.75	902.2
$ZnFe_2O_4$	58.3	0.551	4.46	
$ZnFe_2O_4$/MNC	19.2	0.097	1.84	1139.0

It is worth noting that SAR of $Mn_xZn_{1-x}Fe_2O_4$/MNC is the highest, reported so far for MNPs around 10 nm.[16,17,19,31,45] However, $Mn_xZn_{1-x}Fe_2O_4$ does not show any improved magnetic properties such as M_s compared to the literature.[17] The dipole−dipole interactions of MNPs in spherical clusters may enhance SAR by improving effective magnetic moment of MNPs. The similar behavior was reported by Gazeau et al., who found that SAR of multicore MNPs was 3- to 11-fold of single-core MNPs because of enhanced dipole−dipole interactions in multicore samples.[28] When we compared to multicore MNPs, the advantage of self-assembled MNPs clusters is twofold: it is easier to prepare and it has more potential in tumor multitreatment by loading with hydrophobic drug simultaneously.[46]

3.5. In Vitro Biocompatibility of Micellar $Mn_xZn_{1-x}Fe_2O_4$/MNCs. The biocompatibility of the micellar $Mn_xZn_{1-x}Fe_2O_4$/MNCs was investigated by MTT and CLSM. MCF-7 and MCF-7/ADR were used to study the cytotoxicity of those micellar MNCs.

After 48 h incubation with micellar $Mn_xZn_{1-x}Fe_2O_4$/MNCs, survival rate of MCF-7 is shown in Figure 7A, which indicates good biocompatibility of those micelles in the concentration range of 0.05−1.00 mg mL^{-1}. $MnFe_2O_4$/MNC, $Mn_{0.8}Zn_{0.2}Fe_2O_4$/MNC, and $Mn_{0.6}Zn_{0.4}Fe_2O_4$/MNC all display excellent biocompatibility, as their cell survival rates approximate or even exceed 100% at the highest concentrations. The fluorescence imaging of MCF-7, incubated with different micellar MNCs at the highest concentration of 1 mg mL^{-1}, observed by CLSM, is shown in Figure 7B. MCF-7 was stained with DAPI for nucleus and DiI for cell membrane simultaneously. The fluorescence imaging confirms their good biocompatibility visually. Apparently, integrity of cell morphology was not influenced by micellar MNCs of high concentration, as intact red cell membranes are around blue nucleus. After 48 h of incubation with different micellar MNCs, cells exhibit good proliferative activity, as their morphology and nuclear/cytoplasmic ratio are highly similar as those of control.

The $Mn_xZn_{1-x}Fe_2O_4$/MNCs also show excellent biocompatibility on MCF-7/ADR. MTT results show their cell viability approximate or even exceed 100% at different concentrations, as shown in Figure 7C. It is possible that MCF-7/ADR is resistant to the adverse condition, such as drugs or other therapeutic agents. The fluorescence imaging of MCF-7/ADR also indicates excellent biocompatibility of micellar $Mn_xZn_{1-x}Fe_2O_4$/MNCs. Upon interaction with the micellar $Mn_xZn_{1-x}Fe_2O_4$/MNCs, MCF-7/ADR displays thicker cell membrane and larger nuclear/cytoplasmic ratio than that of MCF-7, as shown in Figure 7D.

3.6. Optimization of the AMF Parameters for Magnetic Hyperthermia. $MnFe_2O_4$/MNC and $Mn_{0.6}Zn_{0.4}Fe_2O_4$/MNC were investigated for efficiency of MFH. The former was selected for its highest SAR, excellent

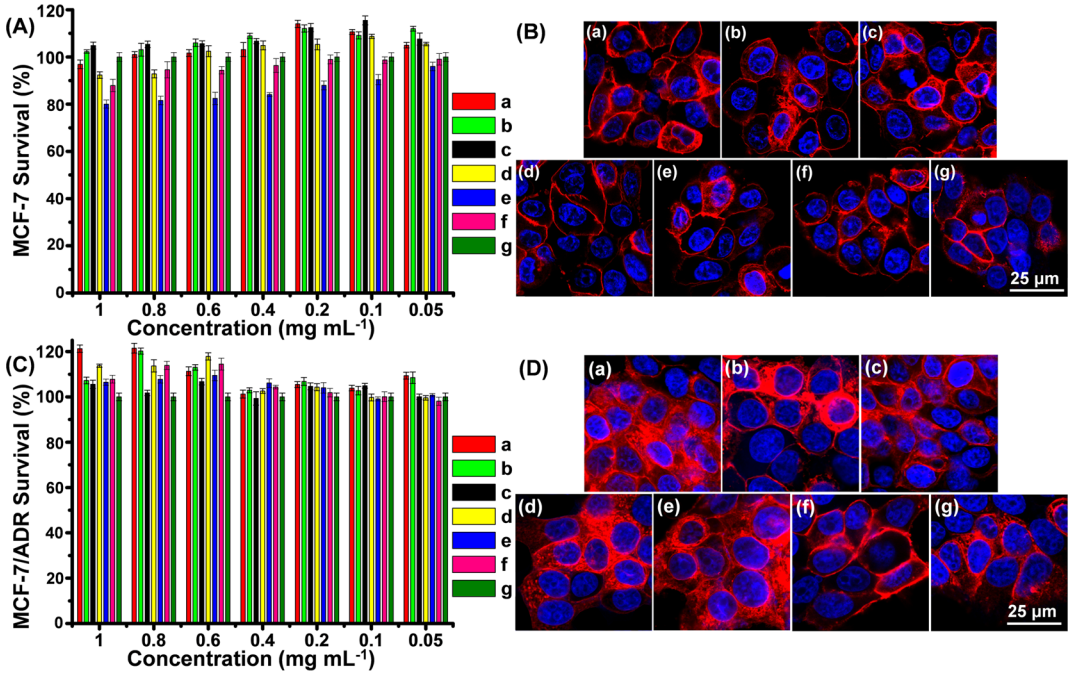

Figure 7. Cytotoxicity of $Mn_xZn_{1-x}Fe_2O_4$/MNCs on MCF-7 and MCF-7/ADR: (A) MTT result of MCF-7; (B) fluorescence imaging of MCF-7; (C) MTT result of MCF-7/ADR; and (D) fluorescence imaging of MCF-7/ADR; (a) $MnFe_2O_4$/MNC, (b) $Mn_{0.8}Zn_{0.2}Fe_2O_4$/MNC, (c) $Mn_{0.6}Zn_{0.4}Fe_2O_4$/MNC, (d) $Mn_{0.4}Zn_{0.6}Fe_2O_4$/MNC, (e) $Mn_{0.2}Zn_{0.8}Fe_2O_4$/MNC, (f) $ZnFe_2O_4$/MNC, and (g) control.

magnetic property, and biocompatibility. The latter exhibited the highest M_s and excellent magnetocaloric effect for potential applications in magnetic targeting and MRI.

For enhanced SAR and biocompatibility, the concentration of $MnFe_2O_4$/MNC and $Mn_{0.6}Zn_{0.4}Fe_2O_4$/MNC was optimized to be 0.2 mg mL^{-1}, of which the MNPs was about 0.1 mg mL^{-1}.

The magnetocaloric effect of $MnFe_2O_4$/MNC is more pronounced than that of $Mn_{0.6}Zn_{0.4}Fe_2O_4$/MNC in medium, as shown in Figure 8. The initial calefactive velocity and maximum self-heating temperature are also shown in this figure. As can be seen, the initial calefactive velocity and the maximum self-heating temperature of $MnFe_2O_4$/MNC and $Mn_{0.6}Zn_{0.4}Fe_2O_4$/MNC all increase with increasing $H_{applied}$. The calefactive velocities of $MnFe_2O_4$/MNC and $Mn_{0.6}Zn_{0.4}Fe_2O_4$/MNC are found to be too fast and overheating at an AMF of 114.6 kA m^{-1}. But their counterparts exhibit calefactive velocities that are too slow under an AMF of 62.8 kA m^{-1}. $H_{applied}$ of AMF was determined to be 89.9 kA m^{-1}. However, the maximum self-heating temperatures of $MnFe_2O_4$/MNC and $Mn_{0.6}Zn_{0.4}Fe_2O_4$/MNC were much higher than 43 °C at an AMF of 89.9 kA m^{-1}. As a result, the exposure time to cancer cell under AMF has to be balanced between safety and efficiency of MFH.

3.7. Efficiency of MFH and the Mechanism of Cell Death Induced by MFH. In the study of hyperthermia, cell survival has shown a typical "shoulder" that reflects a two-step process of cell killing.[43] The first step is characterized by a gentle slope in the beginning of heat exposure, showing a reversible and nonlethal heat damage of cell. The following step displays a sharp slope indicating exponential cell death. The critical transition to the exponential phase needs a particular thermal dose, which is closely correlated to the cellular protein denaturation and an amount of 140 kcal mol^{-1}, calculated by the in vitro and in vivo studies.[47] The key factor to induce cell

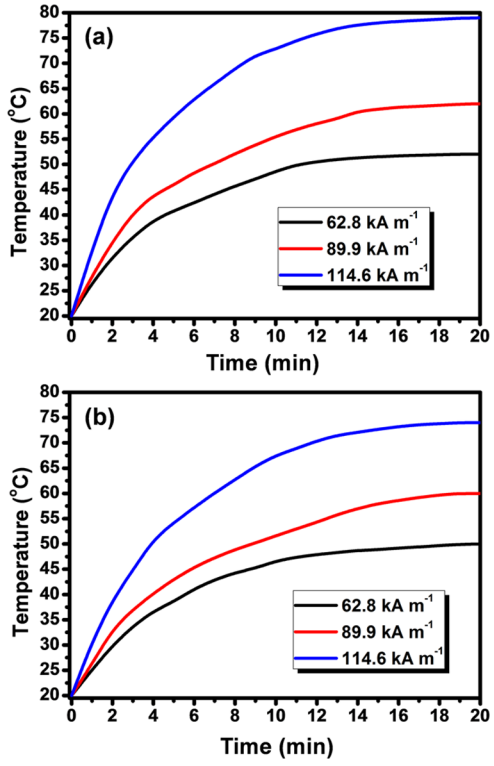

Figure 8. Time-dependent temperature curves of $MnFe_2O_4$/MNC and $Mn_{0.6}Zn_{0.4}Fe_2O_4$/MNC in medium under AMF of different $H_{applied}$: (a) $MnFe_2O_4$/MNC and (b) $Mn_{0.6}Zn_{0.4}Fe_2O_4$/MNC.

death is thermal dose, which has been described as the energy required for cell death "during a certain exposure time (t) at a given temperature (T)".[48] However, the magnetic fluid of high SAR can induce continuous temperature rise with the increasing exposure time under AMF. Therefore, the temper-

dx.doi.org/10.1021/am5042934 | ACS Appl. Mater. Interfaces 2014, 6, 16867−16879

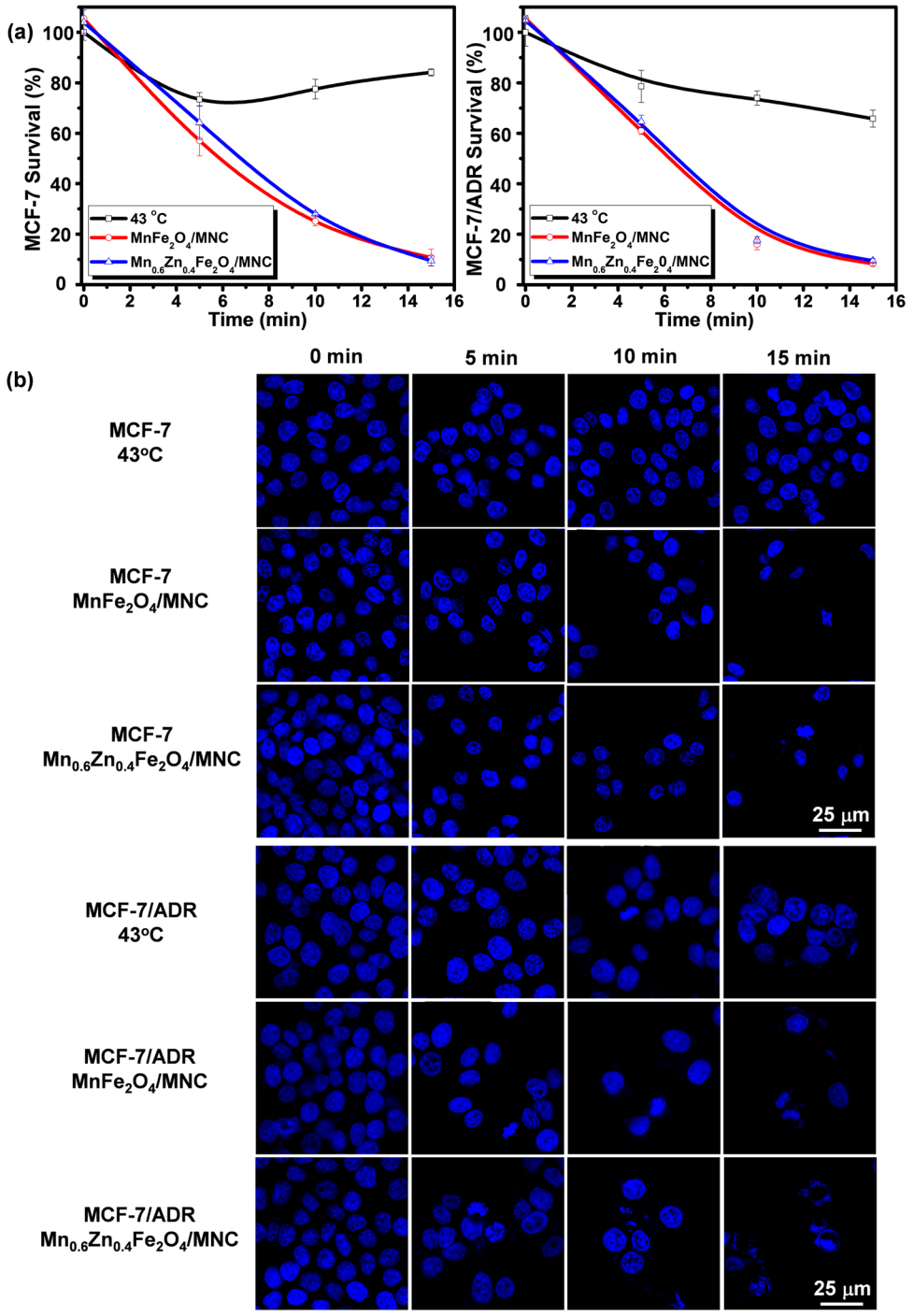

Figure 9. Cytotoxicity of MFH and mild hyperthermia on MCF-7 and MCF-7/ADR with different exposure times: (a) MTT result of MCF-7 and MCF-7/ADR, and (b) fluorescence imaging of MCF-7 and MCF-7/ADR.

ature is often higher than the given level in traditional hyperthermia (≈43 °C). As shown in Figure 8, the temperatures of $MnFe_2O_4$/MNC and $Mn_{0.6}Zn_{0.4}Fe_2O_4$/MNC were found to rise rapidly above 43 °C only several minutes (≤5 min) after application of AMF. Consequently, the efficiency of MFH can be improved significantly with much less exposure time for exponential cell death.

In this study, the efficiency of MFH was investigated with different exposure times of 5, 10, and 15 min. This experiment was carried out to compare with the efficiency of standard hyperthermia at 43 °C for the same exposure times. The efficiency of MFH was evaluated for both MCF-7 and MCF-7/ADR on treatment of drug-sensitive and drug-resistive cancer cells. Moreover, the pathway of cell death was investigated for identifying the mechanism of MFH.

The efficiency of MFH was evaluated by MTT and fluorescence imaging. In Figure 9, the MTT results show similar survival trends of MCF-7 and MCF-7/ADR at 24 h posthyperthermia. Both $MnFe_2O_4$/MNC and $Mn_{0.6}Zn_{0.4}Fe_2O_4$/MNC have rapidly suppressed the cell viability with increasing exposure time under AMF. The survivals of MCF-7 and MCF-7/ADR have decreased to 10%

Table 2. Apoptotic Assay of MCF-7, Induced by Mild Hyperthermia (43 °C) and MFH ($MnFe_2O_4$/MNC and $Mn_{0.6}Zn_{0.4}Fe_2O_4$/MNC)

	43 °C				MFH by $MnFe_2O_4$/MNC				MFH by $Mn_{0.6}Zn_{0.4}Fe_2O_4$/MNC			
	0 min	5 min	10 min	15 min	0 min	5 min	10 min	15 min	0 min	5 min	10 min	15 min
Q1	95.7%	88.5%	87.4%	80.0%	99.2%	77.8%	35.2%	13.8%	99.8%	78.7%	40.5%	16.9%
Q2	4.07%	9.51%	11.7%	13.8%	0.05%	20.7%	43.4%	41.7%	0.05%	19.8%	45.1%	36.7%
Q3	0.03%	1.70%	0.86%	5.97%	0.00%	1.43%	20.1%	43.2%	0.00%	1.43%	12.8%	42.8%
Q4	0.19%	0.27%	0.05%	0.27%	0.79%	0.06%	1.33%	1.31%	0.15%	0.07%	1.54%	3.51%

Table 3. Apoptotic Assay of MCF-7/ADR, Induced by Mild Hyperthermia (43 °C) and MFH ($MnFe_2O_4$/MNC and $Mn_{0.6}Zn_{0.4}Fe_2O_4$/MNC)

	43 °C				MFH by $MnFe_2O_4$/MNC				MFH by $Mn_{0.6}Zn_{0.4}Fe_2O_4$/MNC			
	0 min	5 min	10 min	15 min	0 min	5 min	10 min	15 min	0 min	5 min	10 min	15 min
Q1	93.1%	83.4%	79.6%	75.5%	93.9%	75.2%	20.3%	10.2%	94.8%	75.1%	25.0%	11.0%
Q2	6.24%	11.9%	15.1%	21.7%	5.51%	17.1%	50.3%	33.4%	4.73%	18.1%	48.4%	41.1%
Q3	0.48%	4.20%	4.74%	2.41%	0.36%	5.51%	26.6%	52.1%	0.32%	5.65%	25.2%	44.0%
Q4	0.20%	0.49%	0.58%	0.20%	0.19%	2.16%	2.74%	4.29%	0.15%	1.07%	1.39%	3.93%

under AMF for 15 min. In contrast, the standard hyperthermia at 43 °C showed the mild cytotoxicity and even induced the thermotolerance of MCF-7, as shown in Figure 9a. The survival rate of MCF-7 decreases to 80% in 5 min, then increases slightly with increasing time. Meanwhile, the survival of MCF-7/ADR decreases slowly with increasing time at 43 °C, which is significantly higher than those under MFH.

The decrease of cell numbers at 24 h posthyperthermia can be visualized from the fluorescence imaging of MCF-7 and MCF-7/ADR, as shown in Figure 9b. The nucleuses of the living cells were dyed by DAPI to exhibit blue fluorescence, whereas dead cells fell off from cell culture dish without staining. MFH was found to induce cell death exponentially with increasing exposure time. However, the number of living cells remained at a much higher level when treated by standard hyperthermia (43 °C), for the same exposure time.

The pathways of cell death were studied by staining with Annexin-V-FITC/PI, and measured by flow cytometry.[49] As is well-known, as nucleus dye, PI is unable to penetrate intact membranes of living cells, whereas necrosis cells can be stained by PI. Annexin-V-FITC is another marker to indicate apoptosis cells since Annexin-V can interact strongly and specifically with exposed phosphatidylserine (PS). PS usually locates inside of the lipid bilayer in living cells, and is transported to outside membrane surface of the apoptosis cells.[50] In the early stage of apoptosis, the apoptosis cells can be stained by Annexin-V-FITC only, because they maintain intact membranes without permeating PI. However, in the late stage, the apoptosis cells can be stained by both Annexin-V-FITC and PI, as they are broken apart into several vesicles called apoptotic bodies which lack intact membranes. Therefore, the status of cells and pathways of cell death can be distinguished by analyzing fluorescence intensity of FITC (green light) and PI (red light) of each cell, as shown in Supporting Information Figure S4. The cells with different status are distributed in 4 quadrants, in which Q1 represents the living cells with Annexin-V-FITC-/PI-, Q2 as early stage apoptosis cells with Annexin-V-FITC+/PI-, Q3 the late stage apoptosis cells with Annexin-V-FITC+/PI+, and Q4 the debris of necrosis cells with Annexin-V-FITC-/PI+ (as depicted in Scheme 1), as listed in Table 2 (MCF-7) and Table 3 (MCF-7/ADR).

Similar to negative control (43 °C for 0 min in Tables 2 and 3), MCF-7 and MCF-7/ADR are distributed in Q1 with great viability after 24 h incubation with $MnFe_2O_4$/MNC (0 min) and $Mn_{0.6}Zn_{0.4}Fe_2O_4$/MNC (0 min). Upon different treatments, MCF-7 and MCF-7/ADR are gradually shifted from Q1 to Q2 with pronounced increase of FITC fluorescent intensity (Supporting Information Figure S4). For prolonged exposure time, the cells are gradually shifted from Q2 to Q3 with obvious increase of PI fluorescent intensity (Supporting Information Figure S4). However, as a positive control, standard hyperthermia (43 °C) can induce slow increase of FITC and PI fluorescent intensity in cells. Compared with the positive control, MFH is much more efficient to induce cell apoptosis. As shown in Tables 2 and 3, MFH decreases the number of living cells quickly, and the number of apoptosis cells increases with the corresponding rate. As exposure time increases, the number of apoptosis cells increases more rapidly. Meanwhile, the apoptosis cells gradually develop from the early stage to late stage. The results of flow cytometry are consistent with MTT data and fluorescence imaging.

The behaviors of cell apoptosis induced by both micellar MNCs are similar, but the efficiency of $MnFe_2O_4$/MNC appears better than that of $Mn_{0.6}Zn_{0.4}Fe_2O_4$/MNC according to the data shown in Tables 2 and 3. After 10 min MFH, proportions of MCF-7 and MCF-7/ADR in Q1 by $MnFe_2O_4$/MNC are lower than those of $Mn_{0.6}Zn_{0.4}Fe_2O_4$/MNC. The gaps of cell proportion in Q1 between both micellar MNCs narrow down with the increasing of exposure time (15 min). The development of cell apoptosis by $MnFe_2O_4$/MNC, however, is seen to be faster than that by $Mn_{0.6}Zn_{0.4}Fe_2O_4$/MNC. For MCF-7, the proportion of cell apoptosis (Q2 + Q3) is slightly higher by $MnFe_2O_4$/MNC than that by $Mn_{0.6}Zn_{0.4}Fe_2O_4$/MNC. For MCF-7/ADR, the proportion of late stage apoptosis (Q3) by $MnFe_2O_4$/MNC (15 min, 52.1%) is higher than its counterpart by $Mn_{0.6}Zn_{0.4}Fe_2O_4$/MNC (15 min, 44.0%). Even SAR of $MnFe_2O_4$/MNC (1618 W g^{-1}) is higher than that of $Mn_{0.6}Zn_{0.4}Fe_2O_4$/MNC (1102 W g^{-1}); their MFH efficiencies are comparable, as evidenced in the proportions of living cells. It is likely that they provide sufficient thermal energies to induce cell apoptosis; therefore, both can serve as effective candidates for MFH. As the SARs of $Mn_xZn_{1-x}Fe_2O_4$/MNC (x = 0−0.8) are close to those of $Mn_{0.6}Zn_{0.4}Fe_2O_4$/MNC (shown in Table 1), other $Mn_xZn_{1-x}Fe_2O_4$/MNC can also be appropriate candidates for MFH.

It is to be noted that debris of less necrosis cells is observed, as shown in Tables 2 and 3, even for MCF-7 and MCF-7/ADR treated by 15 min MFH. A previous study indicated the increase of self-heating temperatures of $MnFe_2O_4$/MNC and $Mn_{0.6}Zn_{0.4}Fe_2O_4$/MNC to, respectively, 45.9/43, 55.5/51.6, and 60.9/57 °C, for the exposure times of 5, 10, and 15 min under AMF (shown in Figure 8). MFH of $MnFe_2O_4$/MNC and $Mn_{0.6}Zn_{0.4}Fe_2O_4$/MNC can inevitably lead to overheating, which is a potential risk for patients. To avoid overheating, previous studies have reduced the concentration of MNPs,[18,28,35,51,52] or adjusted parameters of AMF to maintain temperature of MFH in the range of 43−45 °C,[18,35,52] which was considered the optimal temperature for hyperthermia. Meanwhile, in those studies, AMF was typically applied on cells for 1 h for effective MFH, which resulted in cell death of 50%−70%.[18,28,35,51,52] Among all previous reports, a few investigated the pathway of cell death. Cheon et al. found cell apoptosis induced by GdTx MNPs under AMF at 43 °C for 1 h with a total fatality rate of cancer cells of 57%.[52] The fatality rates of cancer cells were found to be much higher in this study, compared to the previously reported studies, however, with less MFH exposure time. Furthermore, the predominant cell death pathway of MCF-7 and MCF-7/ADR was identified as cell apoptosis.

4. CONCLUSIONS

We have successfully synthesized monodispersed $Mn_xZn_{1-x}Fe_2O_4$ magnetic nanoparticles of 8 nm and encapsulated them in amphiphilic block copolymer as micellar $Mn_xZn_{1-x}Fe_2O_4$/MNCs for efficient MFH. These micellar MNCs have been characterized as superparamagnetic materials with high SAR and M_s. The experimental findings have shown their excellent stability and biocompatibility. On the basis of those findings, $MnFe_2O_4$/MNC and $Mn_{0.6}Zn_{0.4}Fe_2O_4$/MNC are selected for further studies. To ensure biosafety of MFH, AMF parameters have been optimized with low f and adjustable $H_{applied}$ for less exposure time according to the cell death mechanism. Under optimized conditions, MFH of $MnFe_2O_4$/MNC and $Mn_{0.6}Zn_{0.4}Fe_2O_4$/MNC have shown induced cancer cell death up to 90% within 15 min. The pathway of cancer cell death is identified as apoptosis, which occurs in mild hyperthermia around 43 °C. Both $MnFe_2O_4$/MNC and $Mn_{0.6}Zn_{0.4}Fe_2O_4$/MNC have shown similar efficiencies on drug-sensitive and drug-resistant cancer cells. On the basis of the experimental results of this study, the micellar $Mn_xZn_{1-x}Fe_2O_4$/MNCs will show promise in future medical applications of cell targeting, cancer diagnosis, and MFH. Furthermore, the multimodal cancer treatment is also possible as amphiphilic block copolymer can encapsulate MNPs, hydrophobic drug, and other functional molecules.

■ ASSOCIATED CONTENT

Supporting Information

Elemental analysis of $Mn_xZn_{1-x}Fe_2O_4$ (EDS and ICP-AES results), ^1H NMR spectrum of mPEG−PCL, magnetic property of micellar $Mn_xZn_{1-x}Fe_2O_4$/MNCs, and cell apoptotic analysis induced by different hyperthermia. This material is available free of charge via the Internet at http://pubs.acs.org.

■ AUTHOR INFORMATION

Corresponding Authors

*Tel./fax: +86-21-69580234. E-mail: renjie6598@163.com.
*Tel./fax: +86-21-33515906. E-mail: lijianbo@tongji.edu.cn.

Notes

The authors declare no competing financial interest.

■ ACKNOWLEDGMENTS

The authors acknowledge the financial support from the National High Technology Research and Development Program of China (No.2013AA032202), the Science and Technology Commission of Shanghai Municipality (No.11 nm0505100), the National Natural Science Foundation of China (No. 51203118), the Fundamental Research Funds for the Central Universities, and the Open Funds for Characterization of Tongji University.

■ REFERENCES

(1) Schildkopf, P.; Ott, O. J.; Frey, B.; Wadepohl, M.; Sauer, R.; Fietkau, R.; Gaipl, U. S. Biological Rationales and Clinical Applications of Temperature Controlled Hyperthermia—Implications for Multimodal Cancer Treatments. *Curr. Med. Chem.* **2010**, *17*, 3045−3057.
(2) Roti Roti, J. L. Cellular Responses to Hyperthermia (40−46 °C): Cell Killing and Molecular Events. *Int. J. Hyperthermia* **2008**, *24*, 3−15.
(3) van der Zee, J.; González González, D.; van Rhoon, G. C.; van Dijk, J. D.; van Putten, W. L.; Hart, A. A. Comparison of Radiotherapy Alone with Radiotherapy Plus Hyperthermia in Locally Advanced Pelvic Tumours: A Prospective, Randomised, Multicentre Trial. *Lancet* **2000**, *355*, 1119−1125.
(4) Shanmugam, V.; Chien, Y. H.; Cheng, Y. S.; Liu, T. Y.; Huang, C. C.; Su, C.-H.; Chen, Y.-S.; Kumar, U.; Hsu, H. F.; Yeh, C. S. Oligonucleotides—Assembled Au Nanorod-Assisted Cancer Photothermal Ablation and Combination Chemotherapy with Targeted Dual-Drug Delivery of Doxorubicin and Cisplatin Prodrug. *ACS Appl. Mater. Interfaces* **2014**, *6*, 4382−4393.
(5) Kalland, T.; Dahlquist, I. Effects of in Vitro Hyperthermia on Human Natural Killer Cells. *Cancer Res.* **1983**, *43*, 1842−1846.
(6) Frey, B.; Weiss, E. M.; Rubner, Y.; Wunderlich, R.; Ott, O. J.; Sauer, R.; Fietkau, R.; Gaipl, U. S. Old and New Facts about Hyperthermia-Induced Modulations of the Immune System. *Int. J. Hyperthermia* **2012**, *28*, 528−542.
(7) Liu, X.; Huang, N.; Li, H.; Wang, H.; Jin, Q.; Ji, J. Multidentate Polyethylene Glycol Modified Gold Nanorods for in Vivo Near-Infrared Photothermal Cancer Therapy. *ACS Appl. Mater. Interfaces* **2014**, *6*, 5657−5668.
(8) Thomas, C. R.; Ferris, D. P.; Lee, J. H.; Choi, E.; Cho, M. H.; Kim, E. S.; Stoddart, J. F.; Shin, J.-S.; Cheon, J.; Zink, J. I. Noninvasive Remote-controlled Release of Drug Molecules in Vitro Using Magnetic Actuation of Mechanized Nanoparticles. *J. Am. Chem. Soc.* **2010**, *132*, 10623−10625.
(9) Agarwal, A.; Mackey, M. A.; El-Sayed, M. A.; Bellamkonda, R. V. Remote Triggered Release of Doxorubicin in Tumors by Synergistic Application of Thermosensitive Liposomes and Gold Nanorods. *ACS Nano* **2011**, *5*, 4919−4926.
(10) Creixell, M.; Bohórquez, A. C.; Torres-Lugo, M.; Rinaldi, C. EGFR-targeted Magnetic Nanoparticle Heaters Kill Cancer Cells without a Perceptible Temperature Rise. *ACS Nano* **2011**, *5*, 7124−7129.
(11) Stolik, S.; Delgado, J. A.; Pérez, A.; Anasagasti, L. Measurement of the Penetration Depths of Red and Near Infrared Light in Human "ex Vivo" Tissues. *J. Photochem. Photobiol., B* **2000**, *57*, 90−93.
(12) Huang, J.; Wang, L.; Lin, R.; Wang, A. Y.; Yang, L.; Kuang, M.; Qian, W.; Mao, H. Casein-coated Iron Oxide Nanoparticles for High MRI Contrast Enhancement and Efficient Cell Targeting. *ACS Appl. Mater. Interfaces* **2013**, *5*, 4632−4639.
(13) Yallapu, M. M.; Othman, S. F.; Curtis, E. T.; Gupta, B. K.; Jaggi, M.; Chauhan, S. C. Multi-functional Magnetic Nanoparticles for Magnetic Resonance Imaging and Cancer Therapy. *Biomaterials* **2011**, *32*, 1890−1905.
(14) Hayashi, K.; Nakamura, M.; Sakamoto, W.; Yogo, T.; Miki, H.; Ozaki, S.; Abe, M.; Matsumoto, T.; Ishimura, K. Superparamagnetic

Nanoparticle Clusters for Cancer Theranostics Combining Magnetic Resonance Imaging and Hyperthermia Treatment. *Theranostics* **2013**, *3*, 366−376.
(15) Meffre, A.; Mehdaoui, B.; Kelsen, V.; Fazzini, P. F.; Carrey, J.; Lachaize, S.; Respaud, M.; Chaudret, B. A Simple Chemical Route toward Monodisperse Iron Carbide Nanoparticles Displaying Tunable Magnetic and Unprecedented Hyperthermia Properties. *Nano Lett.* **2012**, *12*, 4722−4728.
(16) Liu, X.-L.; Fan, H.-M.; Yi, J.-B.; Yang, Y.; Choo, E.-S.-G.; Xue, J.-M.; Fan, D.- D.; Ding, J. Optimization of Surface Coating on Fe_3O_4 Nanoparticles for High Performance Magnetic Hyperthermia Agents. *J. Mater. Chem.* **2012**, *22*, 8235−8244.
(17) Jang, J.-T.; Nah, H.; Lee, J.-H.; Moon, S.-H.; Kim, M.-G.; Cheon, J. Critical Enhancements of MRI Contrast and Hyperthermic Effects by Dopant-Controlled Magnetic Nanoparticles. *Angew. Chem., Int. Ed.* **2009**, *48*, 1234−1238.
(18) Guardia, P.; Di Corato, R.; Lartigue, L.; Wilhelm, C.; Espinosa, A.; Garcia-Hernandez, M.; Gazeau, F.; Manna, L.; Pellegrino, T. Water-Soluble Iron Oxide Nanocubes with High Values of Specific Absorption Rate for Cancer Cell Hyperthermia Treatment. *ACS Nano* **2012**, *6*, 3080−3091.
(19) Lee, J.-H.; Jang, J.-T.; Choi, J.-S.; Moon, S.-H.; Noh, S.-H.; Kim, J.-W.; Kim, J.-G.; Kim, I.-S.; Park, K.-I.; Cheon, J. Exchange-Coupled Magnetic Nanoparticles for Efficient Heat Induction. *Nat. Nanotechnol.* **2011**, *6*, 418−422.
(20) Lee, J.-H.; Huh, Y.-M.; Jun, Y.-W.; Seo, J.-W.; Jang, J.-T.; Song, H.-T.; Kim, S.; Cho, E.-J.; Yoon, H.-G.; Suh, J.-S.; Cheon, J. Artificially Engineered Magnetic Nanoparticles for Ultra-sensitive Molecular Imaging. *Nat. Med.* **2007**, *13*, 95−99.
(21) Noh, S.-H.; Na, W.; Jang, J.-T.; Lee, J.-H.; Lee, E.-J.; Moon, S.-H.; Lim, Y.; Shin, J.-S.; Cheon, J. Nanoscale Magnetism Control via Surface and Exchange Anisotropy for Optimized Ferrimagnetic Hysteresis. *Nano Lett.* **2012**, *12*, 3716−3721.
(22) Sun, S.; Zeng, H.; Robinson, D. B.; Raoux, S.; Rice, P. M.; Wang, S.-X.; Li, G. Monodisperse MFe_2O_4 (M = Fe, Co, Mn) Nanoparticles. *J. Am. Chem. Soc.* **2004**, *126*, 273−279.
(23) Zeng, H.; Rice, P. M.; Wang, S.-X.; Sun, S. Shape-Controlled Synthesis and Shape-Induced Texture of $MnFe_2O_4$ Nanoparticles. *J. Am. Chem. Soc.* **2004**, *126*, 11458−11459.
(24) Jana, N. R.; Chen, Y.-F.; Peng, X.-G. Size- and Shape-Controlled Magnetic (Cr, Mn, Fe, Co, Ni) Oxide Nanocrystals via a Simple and General Approach. *Chem. Mater.* **2004**, *16*, 3931−3935.
(25) Lu, J.; Ma, S.; Sun, J.; Xia, C.; Liu, C.; Wang, Z.; Zhao, X.; Gao, F.; Gong, Q.; Song, B.; Shuai, X.; Ai, H.; Gu, Z. Manganese Ferrite Nanoparticle Micellar Nanocomposites as MRI Contrast Agent for Liver Imaging. *Biomaterials* **2009**, *30*, 2919−2928.
(26) Zhang, B.; Li, Q.; Yin, P.; Rui, Y.; Qiu, Y.; Wang, Y.; Shi, D. Ultrasound-Triggered BSA/SPION Hybrid Nanoclusters for Liver-Specific Magnetic Resonance Imaging. *ACS Appl. Mater. Interfaces* **2012**, *4*, 6479−6486.
(27) Pöselt, E.; Kloust, H.; Tromsdorf, U.; Janschel, M.; Hahn, C.; Maßlo, C.; Weller, H. Relaxivity Optimization of a PEGylated Iron-Oxide-Based Negative Magnetic Resonance Contrast Agent for T_2-Weighted Spin-Echo Imaging. *ACS Nano* **2012**, *6*, 1619−1624.
(28) Lartigue, L.; Hugounenq, P.; Alloyeau, D.; Clarke, S. P.; Lévy, M.; Bacri, J. C.; Bazzi, R.; Brougham, D. F.; Wilhelm, C.; Gazeau, F. Cooperative Organization in Iron Oxide Multi-Core Nanoparticles Potentiates their Efficiency as Heating Mediators and MRI Contrast Agents. *ACS Nano* **2012**, *6*, 10935−10949.
(29) Rosensweig, R. E. Heating Magnetic Fluid with Alternating Magnetic Field. *J. Magn. Magn. Mater.* **2002**, *252*, 370−374.
(30) Jeyadevan, B. Present Status and Prospects of Magnetite Nanoparticles-Based Hyperthermia. *J. Ceram. Soc. Jpn.* **2010**, *118*, 391−401.
(31) Peng, E.; Choo, E.-S.; Chandrasekharan, P.; Yang, C.-T.; Ding, J.; Chuang, K.-H.; Xue, J.-M. Synthesis of Manganese Ferrite/Graphene Oxide Nanocomposites for Biomedical Applications. *Small* **2012**, *8*, 3620−3630.
(32) Harmon, B. V.; Corder, A. M.; Collins, R. J.; Gobé, G. C.; Allen, J.; Allan, D. J.; Kerr, J. F. Cell Death Induced in a Murine Mastocytoma by 42−47 °C Heating in Vitro: Evidence that the Form of Death Changes from Apoptosis to Necrosis above a Critical Heat Load. *Int. J. Radiat. Biol.* **1990**, *58*, 845−858.
(33) Li, J.; Qu, Y.; Ren, J.; Yuan, W.; Shi, D. Magnetocaloric Effect in Magnetothermally-Responsive Nanocarriers for Hyperthermia-Triggered Drug Release. *Nanotechnology* **2012**, *23*, 505706.
(34) Natividad, E.; Castro, M.; Goglio, G.; Andreu, I.; Epherre, R.; Duguet, E.; Mediano, A. New Insights into the Heating Mechanisms and Self-Regulating Abilities of Manganite Perovskite Nanoparticles Suitable for Magnetic Fluid Hyperthermia. *Nanoscale* **2012**, *4*, 3954−3962.
(35) Ghosh, R.; Pradhan, L.; Priyabala Devi, Y.; Meena, S. S.; Tewari, R.; Kumar, A.; Sharma, S.; Gajbhiye, N. S.; Vatsa, R. K.; Pandey, B. N.; Ningthoujam, R. S. Induction Heating Studies of Fe_3O_4 Magnetic Nanoparticles Capped with Oleic Acid and Polyethylene Glycol for Hyperthermia. *J. Mater. Chem.* **2011**, *21*, 13388−13398.
(36) Cuong, N. V.; Lia, Y.-L.; Hsieh, M.-F. Targeted Delivery of Doxorubicin to Human Breast Cancers by Folate-Decorated Star-Shaped PEG−PCL Micelle. *J. Mater. Chem.* **2012**, *22*, 1006−1020.
(37) Ma, M.; Wu, Y.; Zhou, J.; Sun, Y.-K.; Zhang, Y.; Gu, N. Size Dependence of Specific Power Absorption of Fe_3O_4 Particles in AC Magnetic Field. *J. Magn. Magn. Mater.* **2004**, *268*, 33−39.
(38) Mosmann, T. Rapid Colorimetric Assay for Cellular Growth and Survival: Application to Proliferation and Cytotoxicity Assays. *J. Immunol. Methods* **1983**, *65*, 55−63.
(39) Schiessl, W.; Potzel, W.; Karzel, H.; Steiner, M.; Kalvius, G. M. Magnetic Properties of the $ZnFe_2O_4$ Spinel. *Phys. Rev. B* **1996**, *53*, 9143−9152.
(40) Bárcena, C.; Sra, A. K.; Chaubey, G. S.; Khemtong, C.; Liu, J.-P.; Gao, J. Zinc Ferrite Nanoparticles as MRI Contrast Agents. *Chem. Commun.* **2008**, *21*, 2224−2226.
(41) Berret, J. F.; Schonbeck, N.; Gazeau, F.; El Kharrat, D.; Sandre, O.; Vacher, A.; Airiau, M. Controlled Clustering of Superparamagnetic Nanoparticles Using Block Copolymers: Design of New Contrast Agents for Magnetic Resonance Imaging. *J. Am. Chem. Soc.* **2006**, *128*, 1755−1761.
(42) Kobayashi, H.; Watanabe, R.; Choyke, P. L. Improving Conventional Enhanced Permeability and Retention (EPR) Effects; What Is the Appropriate Target? *Theranostics* **2014**, *4*, 81−89.
(43) Huang, H. Y.; Hu, S. H.; Hung, S. Y.; Chiang, C. S.; Liu, H. L.; Chiu, T. L.; Lai, H. Y.; Chen, Y. Y.; Chen, S. Y. SPIO Nanoparticle-stabilized PAA-F127 Thermosensitive Nanobubbles with MR/US Dual-Modality Imaging and HIFU-Triggered Drug Release for Magnetically Guided in Vivo Tumor Therapy. *J. Controlled Release* **2013**, *172*, 118−127.
(44) Hua, M. Y.; Yang, H. W.; Liu, H. L.; Tsai, R. Y.; Pang, S. T.; Chuang, K. L.; Chang, Y. S.; Hwang, T. L.; Chang, Y. H.; Chuang, H. C.; Chuang, C. K. Superhigh-Magnetization Nanocarrier as a Doxorubicin Delivery Platform for Magnetic Targeting Therapy. *Biomaterials* **2011**, *32*, 8999−9010.
(45) Hayashi, K.; Ono, K.; Suzuki, H.; Sawada, M.; Moriya, M.; Sakamoto, W.; Yogo, T. High-frequency, Magnetic-Field-Responsive Drug Release from Magnetic Nanoparticle/Organic Hybrid Based on Hyperthermic Effect. *ACS Appl. Mater. Interfaces* **2010**, *2*, 1903−1911.
(46) Qu, Y.; Li, J. B.; Ren, J.; Leng, J. Z.; Lin, C.; Shi, D. L. Enhanced Synergism of Thermo-Chemotherapy by Combining Highly Efficient Magnetic Hyperthermia with Magnetothermally-Facilitated Drug Release. *Nanoscale* **2014**, DOI: 10.1039/C4NR03384A.
(47) Overgaard, J.; Suit, H. D. Time-temperature Relationship the Hyperthermic Treatment of Malignant and Normal Tissue in Vivo. *Cancer Res.* **1979**, *39*, 3248−3253.
(48) Issels, R. D. Hyperthermia Adds to Chemotherapy. *Eur. J. Cancer* **2008**, *44*, 2546−2554.
(49) Ruan, L.; Xu, Z.; Lan, T.; Wang, J.; Liu, H.; Li, C.; Dong, C.; Ren, J. Highly Sensitive Method for Assay of Drug-induced Apoptosis Using Fluorescence Correlation Spectroscopy. *Anal. Chem.* **2012**, *84*, 7350−7358.

(50) Vermes, I.; Haanen, C.; Steffens-Nakken, H.; Reutelingsperger, C. A Novel Assay for Apoptosis Flow Cytometric Detection of Phosphatidylserine Expression on Early Apoptotic Cells Using Fluorescein Labelled Annexin V. *J. Immunol. Methods* **1995**, *184*, 39−51.
(51) Maity, D.; Chandrasekharan, P.; Pradhan, P.; Chuang, K.-H.; Xue, J.-M.; Feng, S.-S.; Ding, J. Novel Synthesis of Superparamagnetic Magnetite Nanoclusters for Biomedical Applications. *J. Mater. Chem.* **2011**, *21*, 14717−14724.
(52) Yoo, D.; Jeong, H.; Preihs, C.; Choi, J.-S.; Shin, T.-H.; Sessler, J. L.; Cheon, J. Double-Effector Nanoparticles: A Synergistic Approach to Apoptotic Hyperthermia. *Angew. Chem., Int. Ed.* **2012**, *51*, 12482−12485.